RSC Advances

PAPER

View Article Online
View Journal | View Issue

Cite this: *RSC Adv.*, 2026, **16**, 8545

Carbon foam derived from co-carbonization of lignin and petroleum asphalt for high-efficiency solar evaporators

Jiawei Shang,[a] Wangda Qu,[b] Chen Liang,[a] Linghong Yin,[b] Ming Li*[a] and Jing Liu[c]

Received 30th December 2025
Accepted 23rd January 2026

DOI: 10.1039/d5ra10093c

rsc.li/rsc-advances

Based on the current low-value applications of petroleum asphalt and the challenges of complex preparation processes and insufficient compressive strength of lignin-based foam carbon materials, a high-performance solar interfacial evaporator (CF2) fabricated through the co-carbonization of lignin and petroleum asphalt is presented. This process exhibits a hierarchically porous carbon foam characterized by low thermal conductivity (0.093 W m^{-1} K^{-1}), outstanding light absorption characteristics (93.31%) and exceptional compressive strength (10.62 MPa). Under 1 standard sunlight, the evaporator achieved a water evaporation rate of 2.04 kg m^{-2} h^{-1} with an evaporation efficiency of 90.59%. During 11 consecutive hours of outdoor desalination testing, CF2 demonstrated inherent salt tolerance, with no crystallization observed on the surface, while producing freshwater that meets WHO standards. This study introduces a novel methodology for developing high-performance, stable materials specifically tailored for interfacial solar desalination applications.

1 Introduction

With the continued growth of the global population and the acceleration of industrialization, the issue of freshwater scarcity is becoming increasingly acute.[1] Current freshwater generation technologies face critical limitations in balancing energy efficiency, cost-effectiveness, and scalability.[2,3] In this context, interfacial solar desalination technology exhibits unique advantages. By constructing a functional photothermal conversion layer on the water surface, solar radiation energy is efficiently converted into thermal energy within the carbon material layer, enabling directional evaporation and separation of interfacial water molecules.[3,4] Compared to traditional desalination processes, this approach reduces thermal energy loss by over 85% through a localized thermal management strategy.[5,6]

As a renewable biomass resource with abundant reserves, lignin demonstrates significant potential in photothermal materials. Its molecular structure features a conjugated aromatic skeleton and active functional groups such as carboxyl, phenolic hydroxyl, and methoxy groups. These characteristics not only enhance photothermal conversion efficiency but also provide an ideal platform for material functionalization modification.[7] Moreover, the high-value utilization of lignin is in line with the current trend of sustainable/solid waste-derived materials.[8,9]

Lignin-based carbon foam has emerged as a research focus for solar interfacial desalination materials due to its three-dimensional porous structure, high specific surface area and excellent photothermal conversion performance.[10] Recent advances in lignin-derived porous carbon materials have further demonstrated their exceptional capabilities for photothermal conversion and solar energy utilization.[11] For instance, Li *et al.* developed a simple and low-cost Janus-type evaporator using potassium hydroxide (KOH)-activated lignin-based carbon materials (KLC) and commercial melamine foam (MF). Under simulated sunlight, this system achieved a water evaporation rate of 1.539 kg m^{-2} h^{-1} with a photothermal conversion efficiency of 95.88%.[12] Similarly, Xi *et al.* fabricated functionalized lignin-based polyurethane foam (LPUF) from enzymatically degraded lignin, achieving a water evaporation rate of 2.58 kg m^{-2} h^{-1}. Surface modification with polyaniline (PANI) further enhanced performance, achieving evaporation rates exceeding 3.0 kg m^{-2} h^{-1}.[13] Liang *et al.* developed a novel carbon foam evaporator synthesized directly from industrial lignin powder *via* pre-oxidation, carbonization, and activation. This system achieved a water evaporation rate of 2.11 kg m^{-2} h^{-1} and a photothermal conversion efficiency of 93.37%.[14] However, these lignin-based carbon foams often exhibit complex preparation processes and limited compressive strength, which may hinder practical application and long-term operational stability.

Petroleum asphalt, a by-product of petroleum refining, exhibits excellent intermediate-phase recombination ability

[a]College of Chemistry and Pharmacy, Qingdao Agricultural University, 700 Changcheng Road, Qingdao, 266109, China. E-mail: liming0414@qau.edu.cn
[b]Laboratory of Lignin-based Materials, College of Life Sciences, Qingdao Agricultural University, Qingdao, 266109, China
[c]College of New Materials and New Energies, Shenzhen Technology University, Shenzhen, 518116, China

during pyrolysis due to its aromatic hydrocarbon/resin components and natural carbonaceous structure.[15] Through heat treatment and activation, it can be transformed into a three-dimensional porous carbon foam.[16] As a novel porous carbon material, petroleum asphalt-based carbon foam shows promising applications in energy, electrode materials, and adsorption due to its high porosity, large specific surface area, chemical stability, and high-temperature resistance.[17,18] For example, Liu *et al.* developed a green, recyclable template method to prepare Fe_3O_4/porous carbon composites (Fe_3O_4/PC) for lithium-ion battery anodes using petroleum asphalt.[19] Wang *et al.* synthesized hierarchical porous carbon materials (HPCs) *via* a one-step carbonization/activation method using petroleum asphalt as a precursor and silica nanorods as templates, successfully applying them to supercapacitors.[20] Huo *et al.* prepared high-specific-surface-area petroleum asphalt-based porous carbon materials using K_2CO_3 chemical activation followed by CO_2 activation.[21] Samuel *et al.* developed nanoporous carbon materials from petroleum asphaltene, demonstrating high specific surface area, thermal stability, and adsorption capacity for hydrogen and carbon dioxide.[22] Despite these advancements, research on the application of petroleum asphalt-based carbon materials as photothermal conversion media in solar-interfaced seawater desalination remains limited.

This study proposes an innovative method that composites renewable lignin with petroleum asphalt, a by-product of industry, and prepares composite carbon foam materials through a co-carbonization process. By reasonably controlling the amount of petroleum asphalt added, the key properties of the composite foam carbon (such as density, microstructure, hydrophilicity, and mechanical strength) can be directionally adjusted, thereby systematically exploring its potential as a high-performance photothermal conversion medium for interfacial solar seawater desalination applications.

2 Experimental

2.1 Materials

Corncob lignin (provided by Longli Biological) and Heavy aromatic oils (derived from the naphthene-base vacuum residue, supplied by CNOOC company). The aromatics content of heavy oil was about 56.4 wt%, while no asphaltene was detected. Sodium chloride (NaCl) was purchased from Macklin (Shanghai, China).

2.2 Experimental procedure

2.2.1 Preparation of lignin. In this experimental procedure, corncob lignin was placed into a ceramic dish and covered with a layer of aluminum foil. Subsequently, the ceramic crucible containing the lignin was then introduced into a GSL-1100X muffle furnace (Kejing Instruments, China). The temperature was increased at a rate of 5 °C min^{-1} and maintained at 240 °C for 2 h of continuous heating. The resulting product was designated as lignin.

2.2.2 Preparation of petroleum asphalt. Heavy aromatic oil was transferred into an alumina crucible, which was subsequently placed into a GSL-1100X muffle furnace (Kejing Instruments, China). The heating rate was set to 3 °C min^{-1}, and the temperature was raised to 310 °C and maintained for 6 h. The softening point of the specimen was determined to be approximately 125.3 ± 5 °C using the ring-and-ball method.

2.2.3 Preparation of carbon foam precursors (F–F3 samples) and carbon foams (CF1and CF2 samples). In this experiment, a specific quantity amount of lignin was mixed with different proportions of petroleum asphalt. The asphalt incorporation ratios were 10%, 30% and 50%. A total mixture mass of 10 g was thoroughly mixed and placed in an alumina crucible. The crucible was covered with aluminum foil and put into a muffle furnace. The furnace was programmed to heat at a rate of 5 °C min^{-1}, reaching a temperature of 450 °C, which was maintained for 1 h. After cooling to room temperature, the samples were designated as F, F1, F2 and F3 corresponding to asphalt incorporation ratios of 0%, 10%, 30% and 50% respectively. Subsequently, F1 and F2 samples were transferred to a KSL-1100X tube furnace (Kejing Instruments, China) for carbonization at 800 °C for 1 h under an argon (Ar) atmosphere, with a heating rate of 3.2 °C min^{-1}. This process yielded carbon foam samples referred to as CF1 and CF2.

2.3 Characterization

Thermogravimetric (TG) analysis of lignin and petroleum asphalt was conducted using a SDT650 simultaneous thermal analyzer (Waters, USA). Approximately 5.00 mg of each sample was heated from room temperature to 1000 °C at a rate of 10 °C min^{-1} under N_2 atmosphere. The softening point of petroleum asphalt was determined using an asphalt softening point tester (Double Star Experimental Instrument, China). Surface functional groups of the samples were analyzed *via* Fourier transform infrared spectroscopy (Thermo Fisher Scientific, Inc., USA) with a scanning range of 750–4000 cm^{-1}. The microstructures of the carbon foam samples were observed using an EOL-7500F scanning electron microscope (SEM, Hitachi, Japan). Compressive properties of the samples were evaluated using a JHY-5000 testing machine (Xiamen Jinheyuan Technology Co., Ltd). The surface wettability of the samples was measured with a contact angle measuring instrument (DSA25S, Kruss, Germany). Reflectance spectra of the samples were analyzed using a UV-visible-near infrared spectrophotometer (UV-3600, Shimadzu, Japan) within a wavelength range of 200–2500 cm^{-1}. Thermal conductivity was analyzed using a thermal conductivity meter (LFA 467 HyperFlash, Germany). The structure of the carbon foams was characterized by XRD (Dandong Tongda Technology Company, China) with a scanning angle of 5°–60°. Raman spectroscopy was conducted on the carbon foam using a 532 nm laser. The carbon foam was analyzed by Raman spectroscopy under 532 nm laser. The concentrations of Na^+, K^+, Ca^{2+}, and Mg^{2+} in natural seawater before and after desalination were determined using inductively coupled plasma mass spectrometry (ICP-MS, PerkinElmer NexION 300X).

The water transfer performance of the samples was evaluated as follows: a 1 cm × 1 cm pH test paper was placed on the

sample surface and subsequently immersed in a Petri dish containing distilled water. The time required for complete wetting of the pH paper was recorded to assess the water transport properties of the samples.

Solar steam generation experiments were conducted using a laboratory self-assembled measurement system. The system comprises the following components: a xenon lamp (PLS-SXE300, Perfect Light, China) equipped with an AM 1.5 filter to simulate sunlight, an electronic balance scale (AH-A, Anheng, China) with an accuracy of 0.001 g to track mass loss during evaporation and an infrared thermal imager (HM-TPH11-3AXF, Hikvision, China) employed to monitor the sample surface temperature. In this experiment, the procedure was as follows: initially, a polyethylene beaker containing 140 g of pure water or 3.5 wt% NaCl solution was placed on an electronic balance. Subsequently, the sample (evaporator) was immersed in the solvent within the beaker. Finally, standard light intensity experiments were performed under the xenon lamp. During this process, the samples were observed to be self-floating. To ensure that evaporation occurred exclusively from the evaporator, the sample surroundings were covered with sponge foam. The experimental environment was maintained at a temperature of 25 ± 3 °C and a humidity level of 50 ± 5%.

The absorption rate (α), evaporation rate (ν), and evaporation efficiency (η) of the sample were calculated according to formulas (1)–(3) in the SI Material. Additionally, the relevant characterization analytical results (Fig. S1–S11) are provided in the SI Materials.

3 Results and discussion

3.1 Structural analysis and desalination performance of F, F1, F2 and F3

The morphological appearance of carbon foam precursors (F, F1, F2, and F3) is shown in Fig. 1(a). All samples were observed as black blocks, which was attributed to the combined effects of decomposition, intra-molecular cross-linking, and softening of lignin and petroleum asphalt during the oxidation phase.[23,24] The bulk densities and oxidation yield of F–F3 samples are presented in Table 1. For the F sample, the bulk density and oxidation yield were 0.556 g cm^{-3} and 60.19%, respectively. This was attributed to the thermal decomposition of lignin during oxidation.[25] The bulk densities of F1, F2, and F3 samples ranged from 0.47 to 0.59 g cm^{-3}, while the corresponding yields ranged from 55 to 61%. This phenomenon indicated that both the bulk density and oxidation yield of carbon foam precursors (F1–F3 samples) exhibited a decreasing trend with increasing proportions of petroleum asphalt. This was primarily attributed to the difference in pyrolysis rates between petroleum asphalt and lignin. As illustrated in Fig. S1, the slope of the TG curve for petroleum asphalt was more pronounced in the temperature range of 250–450 °C compared to lignin, indicating a higher degree of pyrolysis for petroleum asphalt during the oxidation stage. Additionally, the pyrolysis of petroleum asphalt generated gases such as carbon dioxide (CO_2) and methane (CH_4).[26] Since the bulk densities of all F–F3 samples were below 0.60 g cm^{-3}, they satisfied the conditions for solar interfacial

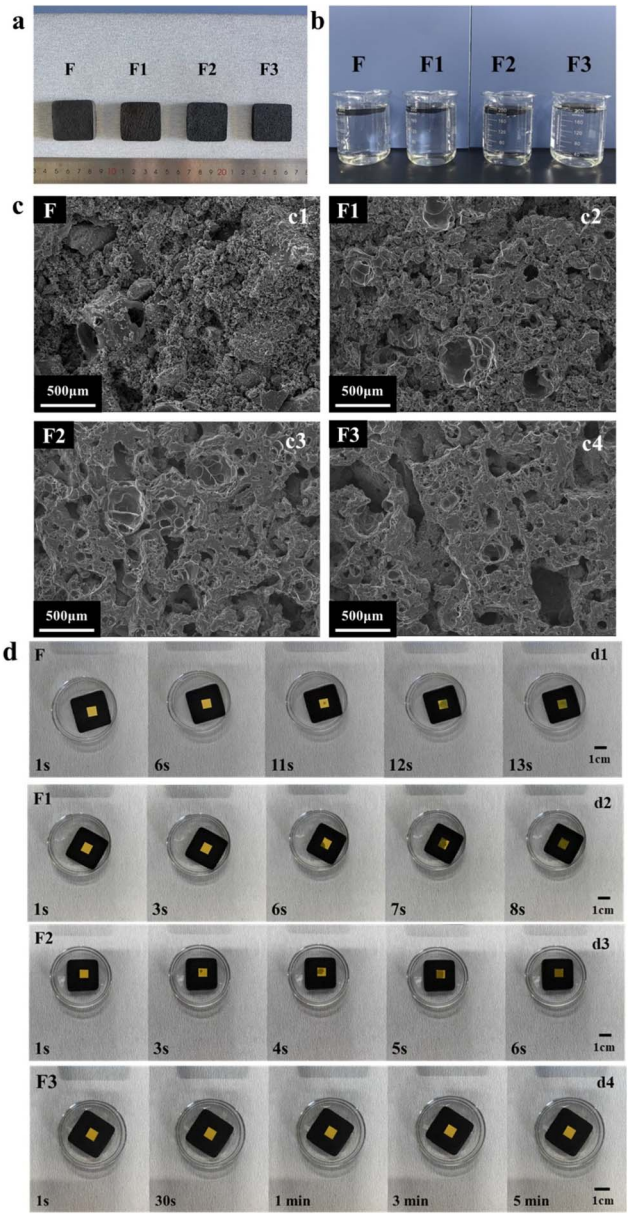

Fig. 1 (a) Appearance morphology of F–F3 samples; (b) the self-floating properties of F–F3 samples; (c) SEM image of F–F3 samples; (d) water transfer permeability test of F–F3 samples.

evaporation. The results are shown in Fig. 1(b), where all F–F3 samples were observed to float on the water surface.

The microstructure of F–F3 samples was investigated using scanning electron microscopy (SEM), and the results are shown in Fig. 1(c). With increasing amounts of petroleum asphalt in the mixture, F–F3 samples gradually developed distinct ligament and pore structures. This was primarily attributed to the softening and pyrolysis of petroleum asphalt during the oxidation process.[26,27] A well-developed ligament structure can enhance the sample's compressive strength, making it suitable for long-term outdoor operation.[28] Porous structural materials are also beneficial for water transport.[29]

In addition, the water transport capacity of the samples significantly influenced their evaporation efficiency. The water

Table 1 The bulk densities and yields of F, F1, F2, F3, CF1 and CF2 samples

Samples	Bulk density (g cm^{-3})	Yield (%)
F	0.556	60.19
F1	0.585	60.16
F2	0.561	57.87
F3	0.477	55.87
CF1	0.610	79.54
CF2	0.640	77.20

transport results are shown in Fig. 1(d). The wetting rate, as measured by pH paper, revealed that the F2 sample exhibited the best water transport performance, followed by F1, F, and F3. This demonstrated that the addition of an appropriate amount of petroleum asphalt could improve the water transport capacity of the samples. This enhancement was attributed to the pyrolysis of petroleum asphalt, which promoted the formation of interconnected pore structures within the samples. As shown in Fig. 1(c1–c4), the pore structure of F–F3 samples gradually evolved with increasing petroleum asphalt content. Simultaneously, the pore walls of the internal pores became thinner and interconnected, providing more flow channels for water and enabling faster water transport within the material.[30] To provide further evidence, the true densities of F, F1, F2, and F3 were investigated, with the results presented in Fig. S2. The measured true densities of F, F1, F2, and F3 are 0.465 g cm^{-3}, 0.549 g cm^{-3}, 0.7157 g cm^{-3}, and 0.9091 g cm^{-3}, respectively, which further corroborate the increasing connectivity of internal pores in the samples.

However, despite its more developed pore structure, the F3 sample exhibited the lowest water transport capacity. This discrepancy may be related to the mixing ratio and physical properties of the asphalt molecules. Petroleum asphalt contained hydrophobic organic compounds, such as alkanes and aromatics.[31,32] At high doping levels (as in F3), these components were incorporated into the material during the synthesis of the carbon foam precursors. This process may have resulted in the formation of a hydrophobic protective layer. To validate this inference, Fourier Transform Infrared (FTIR) spectroscopy was employed to analyze the F–F3 samples. The FTIR results for F–F3 samples are shown in Fig. S3. Compared to F, F1, and F2 samples, the F3 sample exhibited more pronounced absorption peaks at 2970 cm^{-1}, 2900 cm^{-1}, corresponding to the asymmetric stretching vibration of –CH_2– groups in long alkyl chains.[33] Further confirmation was provided by contact angle measurements (Fig. S4). The contact angles of F, F1, and F2 samples were 0° within 0.02 seconds, indicating that these samples were hydrophilic materials. In contrast, the contact angles of the F3 sample were 110° and 108.2° at 1.92 seconds and 10.02 seconds, respectively. This showed that it was a relatively hydrophobic material (contact angle >90°).[34]

The thermal conductivity of the evaporator directly impacts heat transfer efficiency within the system. The thermal conductivities of F, F1, F2, and F3 samples were measured using a thermal conductivity meter and are shown in Fig. S5. The

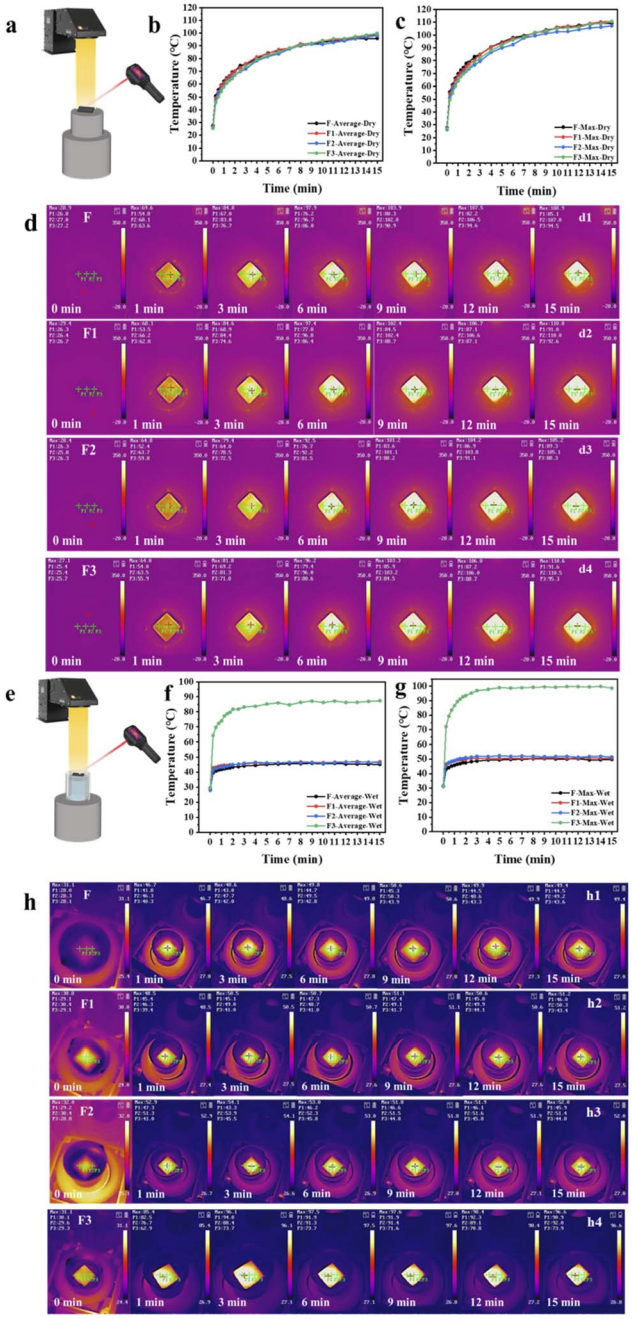

Fig. 2 (a) Generalized diagram of the photothermal conversion device for drying F–F3 samples; (b) average surface temperature change curves of drying F–F3 samples under 1 standard sun; (c) max surface temperature change curves of drying F–F3 samples under 1 standard sun; (d) infrared thermal image of drying F–F3 samples under 1 standard sun; (e) generalized diagram of the photothermal conversion device for wet F–F3 samples; (f) average surface temperature change curves of F–F3 samples in pure water under 1 standard sun; (g) max surface temperature change curves of F–F3 samples in pure water under 1 standard sun; (h) infrared thermal image of F–F3 samples in pure water under 1 standard sun.

thermal conductivities of F, F1, F2, and F3 samples were all less than 0.2 W m^{-1} K^{-1}, respectively, which is lower than many previously reported photothermal materials, thereby minimizing heat loss to the bulk water.[29,35]

To assess the photothermal conversion capability of the sample, a solar radiation experiment was performed on the dry F–F3 sample under standard solar irradiance conditions (1 kW m^{-2}). The experiment lasted for 15 minutes, and the results are presented in Fig. 2 (a–d). Fig. 2(b–d) demonstrate the temperature change curves and infrared thermography images the dried F, F1, F2, and F3 samples during the solar irradiation process. The average surface temperatures rose rapidly, exceeding 70 °C within 3 minutes of irradiation, 80 °C within 6 minutes, and reached 90 °C within 15 minutes. The maximum surface temperature of the F–F3 samples surpassed 95 °C within 10 minutes. These results conclusively demonstrate that the F–F3 samples exhibit exceptional photothermal conversion properties. The superior photothermal conversion performance of the F–F3 samples can be attributed to several factors. First, during heat treatment, petroleum asphalt and lignin undergo a series of reactions, including softening, cross-linking, and pyrolysis, which collectively contribute to the formation of a structurally integrated material.[36] This material possesses a uniform and complete structure, appears black, has low density, low thermal conductivity, and a porous nature, all of which enhance its light-to-heat conversion efficiency. Additionally, the material's molecular structure contains a π–π conjugated system, which reduces the energy barrier for electron transitions, thereby improving the photothermal effect.[37,38]

Furthermore, the average and maximum surface temperatures of the F–F3 sample in pure water were recorded during the first 15 minutes under 1 standard light intensity. The results are shown in Fig. 2(e–h). As irradiation time increased, the average and maximum surface temperatures of the F–F2 samples exhibited minimal changes, rising slightly within the 1 minute before stabilizing. In contrast, the average surface temperature of the F3 sample rapidly increased, exceeding 80 °C within 3 minutes and reaching 87.4 °C at 15 minutes. The maximum surface temperature of the F3 sample reached 90 °C within 6 minutes and surpassed 95 °C within 10 minutes. This disparity confirms the poor water transport in F3 (Fig. 1(d)); the limited water supply prevented effective evaporative cooling, causing heat accumulation.

The compressive strength of the evaporator is critical for adapting to complex environmental conditions, ensuring long-term stable operation, and enhancing efficiency. Therefore, the compressive properties of the F–F3 sample were investigated, and the results are presented in Fig. S6. The compressive strengths of F, F1, F2, and F3 exhibited a trend of increasing from 0.47 to 7.81 MPa, followed by a subsequent decrease to 5.46 MPa. This trend indicates that the compressive strength of the samples initially increases and then decreases with increasing petroleum asphalt content. This behavior is primarily influenced by the softening properties of petroleum asphalt and the mixing ratio. An appropriate proportion of petroleum asphalt enhances the formation of a robust ligament structure within the sample, thereby improving its compressive strength.[18,39] The experimental results presented in Fig. 1(c1–c3) provide a detailed visualization of the ligament structure formation process within the sample. However, when the mixing amount of petroleum asphalt was high, the petroleum asphalt underwent pyrolysis during the oxidation stage, accompanied by the generation of more small molecule gas products. This phenomenon caused significant damage to the internal ligament structure of the sample, leading to a decrease in its compressive strength (Fig. 1c4). It is noteworthy that F1, F2, and F3 samples exhibited excellent compressive strengths

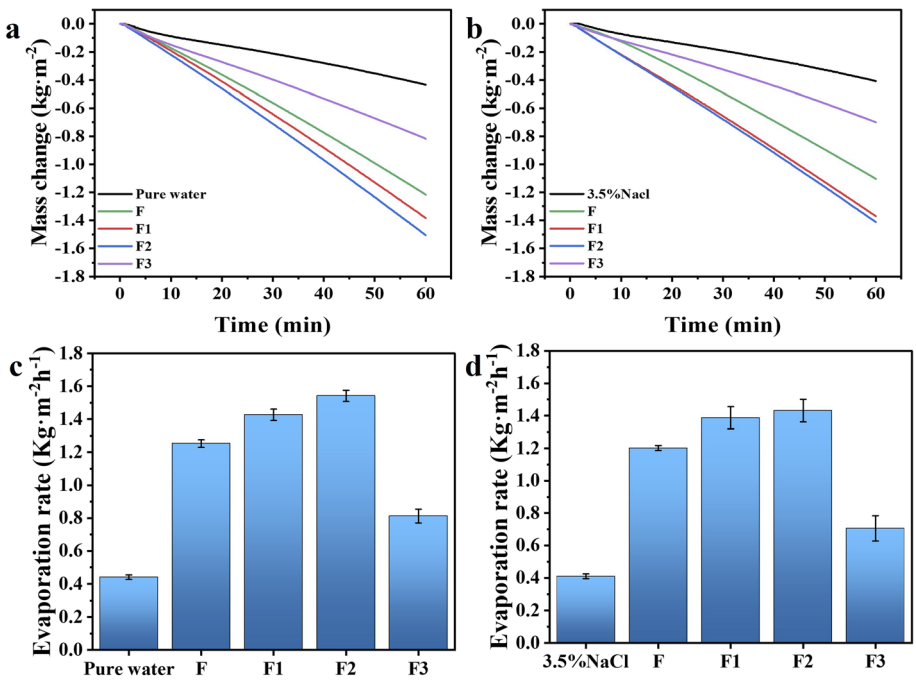

Fig. 3 (a) Evaporation mass change curves in pure water of F–F3 samples under 1 standard sunlight; (b) evaporation mass change curves of F–F3 samples in simulated seawater (3.5% NaCl) under 1 standard sunlight; (c) evaporation rate in pure water of F–F3 samples under 1 standard sunlight; (d) evaporation rate in simulated seawater (3.5% NaCl) of F–F3 samples under 1 standard sunlight.

exceeding 4 MPa. In contrast, previous studies have reported limited data on the compressive strength of evaporator materials, with values typically less than 0.8 MPa,[40,41] although individual cases have occasionally exceeded 1.5 MPa.[14]

The evaporation rate is a critical parameter for assessing the performance of photothermal materials in solar evaporation applications. To evaluate this parameter, experiments were performed on the F–F3 sample utilizing pure water and simulated seawater (3.5% NaCl). As demonstrated in Fig. 3(a) and (c), the evaporation rate exhibited a notable enhancement when F–F2 samples were employed as the evaporator compared to pure water. Under 1 standard sunlight, the evaporation rates of F, F1, F2, and F3 samples were measured to be 1.25 kg m^{-2} h^{-1}, 1.43 kg m^{-2} h^{-1}, 1.55 kg m^{-2} h^{-1} and 0.81 kg m^{-2} h^{-1}, respectively. This trend can be primarily attributed to the previously discussed performance variations among the samples. Further investigations were conducted to assess the evaporation rates of the samples in simulated seawater (3.5% NaCl), with the corresponding results presented in Fig. 3(b) and (d). Notably, the evaporation rates of F–F3 samples in seawater were slightly lower than those in pure water, with recorded values of 1.20 kg m^{-2} h^{-1}, 1.38 kg m^{-2} h^{-1}, 1.43 kg m^{-2} h^{-1} and 0.71 kg m^{-2} h^{-1}, respectively. This reduction was primarily due to the formation of salt crystals on the sample surfaces during the experimental process. As illustrated in Fig. S7, salt crystals were formed on the surface of F–F3 samples in different degrees during the radiation process lasting 1 h. This phenomenon hindered the photothermal conversion efficiency and water transportation channels of the samples.[42] Additionally, this phenomenon could be attributed to the insufficient pore connectivity within the samples.[43,44]

In summary, F1 and F2 samples demonstrated superior application potential as vaporizers compared to F and F3 samples. Their advantages include low density, excellent water transport properties, hydrophilicity, compressive strength, and photothermal conversion ability. However, F1 and F2 samples also exhibited certain limitations. While petroleum asphalt pyrolysis improved the internal pore structure, the enhancements were insufficient to meet the requirements of an ideal evaporator for rapid salt transport, as evidenced by the observed salt crystal precipitation during the experiments. This indicates that there remains significant room for further optimization of F1 and F2 sample performance.

3.2 Structural analysis and desalination performance of CF1 and CF2

Carbonization treatment is performed on F1 and F2 to enable further pyrolysis of materials that were not sufficiently decomposed during the oxidation phase. This process facilitates the

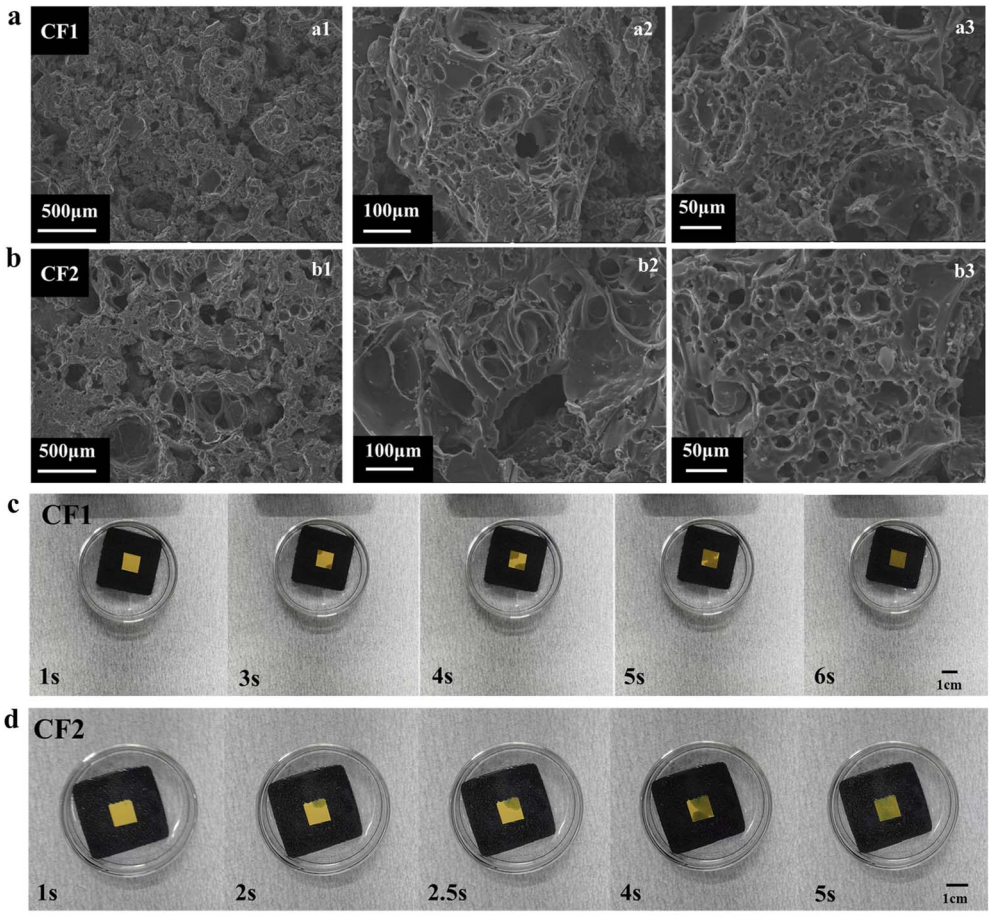

Fig. 4 (a) SEM image of CF1 sample; (b) SEM image of CF2 sample; (c) water transfer permeability test of CF1 sample; (d) water transfer permeability test of CF2 sample.

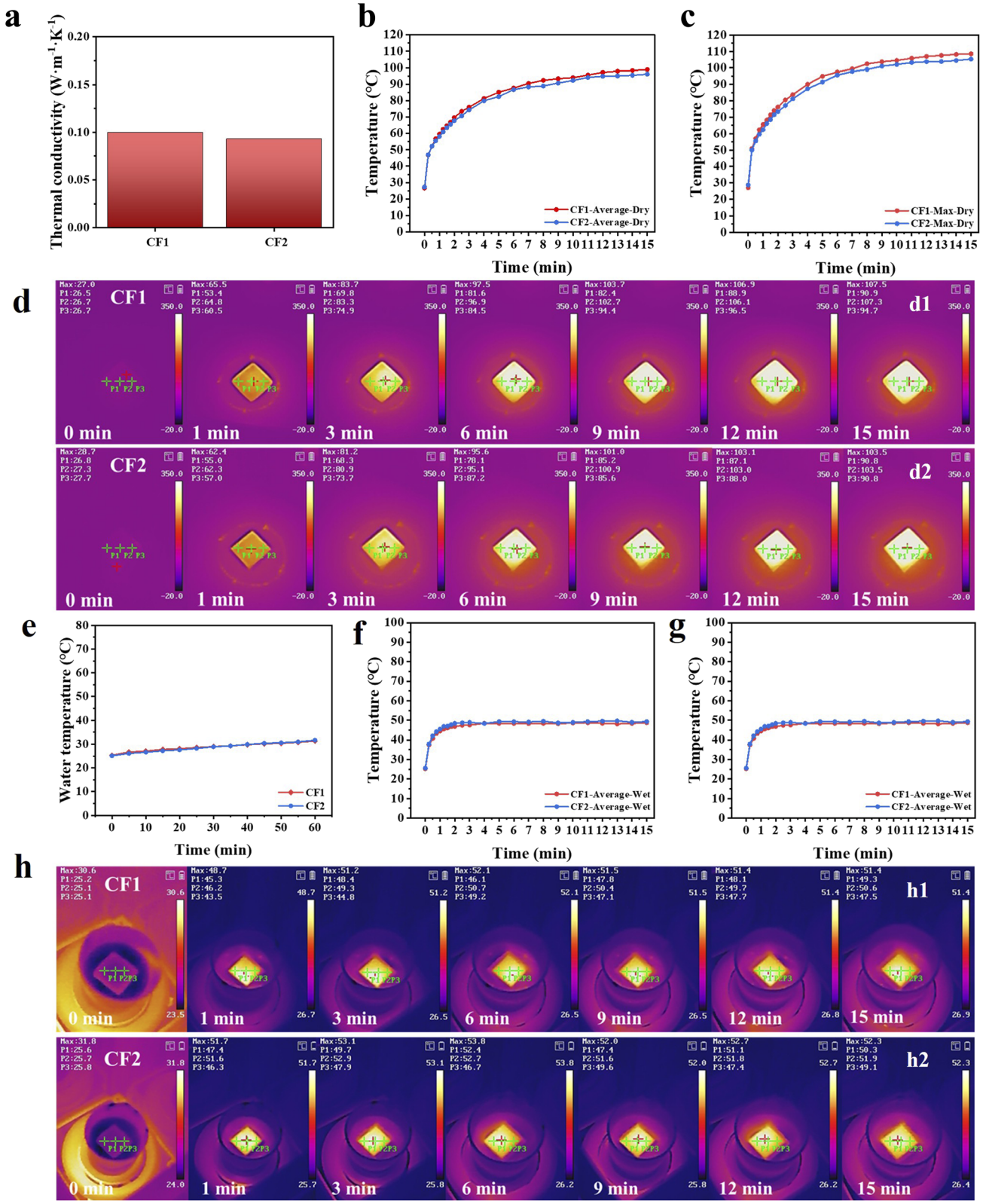

Fig. 5 (a) Thermal conductivity of CF1 and CF2 samples; (b) average surface temperature change curves of drying CF1 and CF2 samples under 1 standard sun; (c) max surface temperature change curves of drying CF1 and CF2 samples under 1 standard sun; (d) infrared thermal image of drying CF1 and CF2 samples under 1 standard sun; (e) change curves in water temperature for CF1 and CF2 samples; (f) average surface temperature change curves of CF1 and CF2 samples in pure water under 1 standard sun; (g) max surface temperature change curves of CF1 and CF2 samples in pure water under 1 standard sun; (h) infrared thermal image of CF1 and CF2 samples in pure water under 1 standard sun.

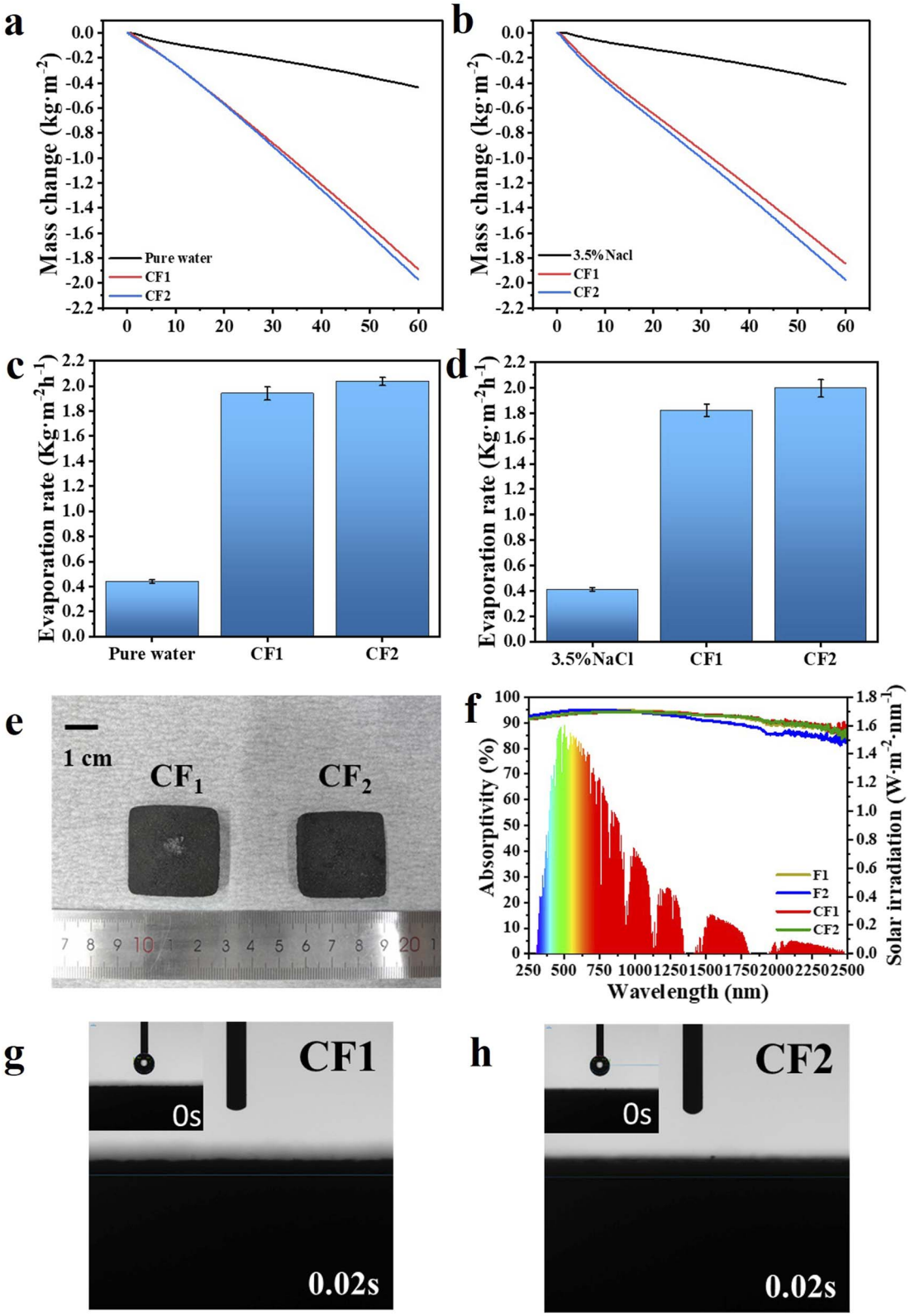

Fig. 6 (a) Evaporation mass change curves in pure water of CF1 and CF2 samples under 1 standard sunlight; (b) evaporation mass curves change of CF1 and CF2 samples in simulated seawater (3.5% NaCl) under 1 standard sunlight; (c) evaporation rate in pure water of CF1 and CF2 samples under 1 standard sunlight; (d) evaporation rate in simulated seawater (3.5% NaCl) of CF1 and CF2 samples under 1 standard sunlight; (e) surface morphology of CF1 and CF2 samples after continuous 1 h radiation in simulated seawater; (f) absorbance of F1, F2, CF1 and CF2 samples; (g) water contact angle for CF1 sample; (h) water contact angle for CF2 sample.

release of pyrolysis gases and structural remodeling, which continuously generates new pore structures within the material.[45,46] Concurrently, this treatment enhances pore connectivity and openness.[23,47] SEM images of CF1 and CF2 samples are presented in Fig. 4(a and b). These results confirm that compared to F1 and F2 samples (Fig. 1c1 and c2), the pore walls of CF1 and CF2 samples are significantly thinner, with improved connectivity. The EDS spectra of F2 and CF2 are presented in Fig. S8, respectively. For F2, the oxygen-to-carbon ratio decreases from an initial value of 0.277 to 0.173 following carbonization. This deoxygenation process facilitates the creation of a through-pore network by liberating gases such as CO_2, thereby opening previously closed pores. Concurrently, the densification of the carbon framework ensures the structural integrity and stability of the pore network.[48] Furthermore, the true densities of CF1 and CF2 are presented in Fig. S9. The true densities of CF1 and CF2 are 1.02 g cm^{-3} and 1.28 g cm^{-3}, respectively, which exhibit further increases compared to F1 and F2. The carbonization yields and densities of CF1 and CF2 samples are summarized in Table 1. The carbonization yields were 79.54% and 77.20% for CF1 and CF2, respectively. This outcome is primarily attributed to the further pyrolysis of substances during the carbonization process. The densities of CF1 and CF2 were 0.61 g cm^{-3} and 0.64 g cm^{-3}, respectively, showing a slight upward trend compared to F1 and F2 samples. This increase is mainly due to the fact that the proportion of volume shrinkage during carbonization, as temperature rises, is lower than the proportion of mass loss.[48,49] The water transfer performance of CF1 and CF2 samples was evaluated, with results shown in Fig. 4(c and d). The pH test paper on the surface of CF1 and CF2 samples became fully wetted within 6 seconds and 5 seconds, respectively, demonstrating their excellent water transfer properties.

The thermal conductivity of CF1 and CF2 samples was further investigated, with results presented in Fig. 5(a). The thermal conductivities were 0.1 W m^{-1} K^{-1} and 0.093 W m^{-1} K^{-1} for CF1 and CF2, respectively, which are comparable to those of recently reported high-performance evaporators (Table S1). This observed reduction in thermal conductivity compared to F1 and F2 samples can be attributed to the increased porosity resulting from the carbonization process. The gas within the pores (typically air) exhibits lower thermal conductivity than the solid carbon material, thereby reducing the overall thermal conductivity.[50,51] Furthermore, the photothermal conversion capacity of CF1 and CF2 samples was assessed. Solar radiation experiments were conducted on dried CF1 and CF2 samples under 1 standard sun intensity (1 kW m^{-2}). After 15 minutes of irradiation, the average and maximum surface temperatures are shown in Fig. 5(b–d). As demonstrated in Fig. 5(b), the average surface temperatures of CF1 and CF2 exceeding 70 °C within 3 minutes, 85 °C within 6 minutes, and 90 °C within 9 minutes. As shown in Fig. 5(c), the maximum surface temperatures of CF1 and CF2 exceeding 80 °C within 3 minutes, 95 °C within 6 minutes, 100 °C within 9 minutes, and 105 °C within 15 minutes. This trend aligns with the results of infrared thermography tests (Fig. 5(d)). The temperature profiles of CF1 and CF2 samples are comparable to those of F1 and F2 samples, confirming their excellent photothermal conversion properties. Surface temperature measurements of CF1 and CF2 samples in pure water under 1 standard sunlight for the first 15 minutes are shown in Fig. 5(f–h). Both the average and maximum surface temperatures of the samples rose within 1 minute and subsequently reached thermal equilibrium. Simultaneously, the water temperature trends during the experiment are presented in Fig. 5(e). The consistent temperature trends for CF1 and CF2 indicate similar heat transfer characteristics to water.

The XRD patterns of CF1 and CF2 are presented in Fig. S10a, revealing two distinct diffraction peaks corresponding to the (002) and (101) peaks, with 2θ values of 23° and 44°, respectively.[52] The calculated d_{002} spacing of the samples ranges from 0.3739 to 0.3700 nm, which is larger than the d_{002} spacing of graphite (0.335 nm). Furthermore, the Raman spectra of the carbon foams are shown in Fig. S10b. The G peak at 1580 cm^{-1} is indicative of sp^2 hybridized structures, reflecting the symmetry and crystallinity of the graphene-based materials. The D peak at 1350 cm^{-1} represents defects and disordered structures within the graphite layers.[14] The peak area ratio of the D peak to the G peak (I_D/I_G) is a widely used parameter to characterize the defect degree of graphite materials. For CF1 and CF2, the I_D/I_G values are 1.82 and 1.73, respectively. This indicates that both CF1 and CF2 have a limited degree of graphitization. The compressive properties of CF1 and CF2 samples were evaluated, with results presented in Fig. S11. The compressive strengths were 5.80 MPa and 10.62 MPa for CF1 and CF2, respectively, indicating a significant improvement in compressive capacity after carbonization. This enhancement is attributed to further cross-linking and softening of the material during the carbonization process, resulting in a tighter bond within the material.[53]

The evaporation rates of CF1 and CF2 samples were evaluated in pure water and simulated seawater (3.5% NaCl). The results are presented in Fig. 6(a–d). Under 1 standard sunlight, the evaporation rates of CF1 and CF2 samples in pure water were 1.94 kg m^{-2} h^{-1} and 2.04 kg m^{-2} h^{-1}, respectively, significantly outperforming most reported evaporators (Table S2). The evaporation rates of CF1 and CF2 samples in simulated seawater (3.5% NaCl) were 1.82 kg m^{-2} h^{-1} and 1.99 kg m^{-2} h^{-1}, respectively. Compared to F1 and F2, the evaporation rates of CF1 and CF2 were significantly enhanced after carbonization. To further investigate the salt crystallization phenomenon, a comparative analysis of the surface properties of the samples was performed. As shown in Fig. 6(e), compared to F1 and F2 samples, the precipitation of salt crystals on the surface of CF1 and CF2 samples was significantly reduced during irradiation lasting 1 hour. Notably, no salt crystal precipitation was observed on the CF2 sample surface. This phenomenon was primarily attributed to the further optimization of the pore structure. The absorbance of F1, F2, CF1, and CF2 samples was measured in the wavelength range of 250–2500 nm. As shown in Fig. 6(f), the absorbance values were 93.93%, 93.61%, 93.31%, and 93.31%, respectively, indicating excellent light absorption capabilities. To evaluate the hydrophilicity of CF1 and CF2, water contact angle tests were conducted. The results are shown in Fig. 6(g and h). Both samples exhibited a contact angle of 0°

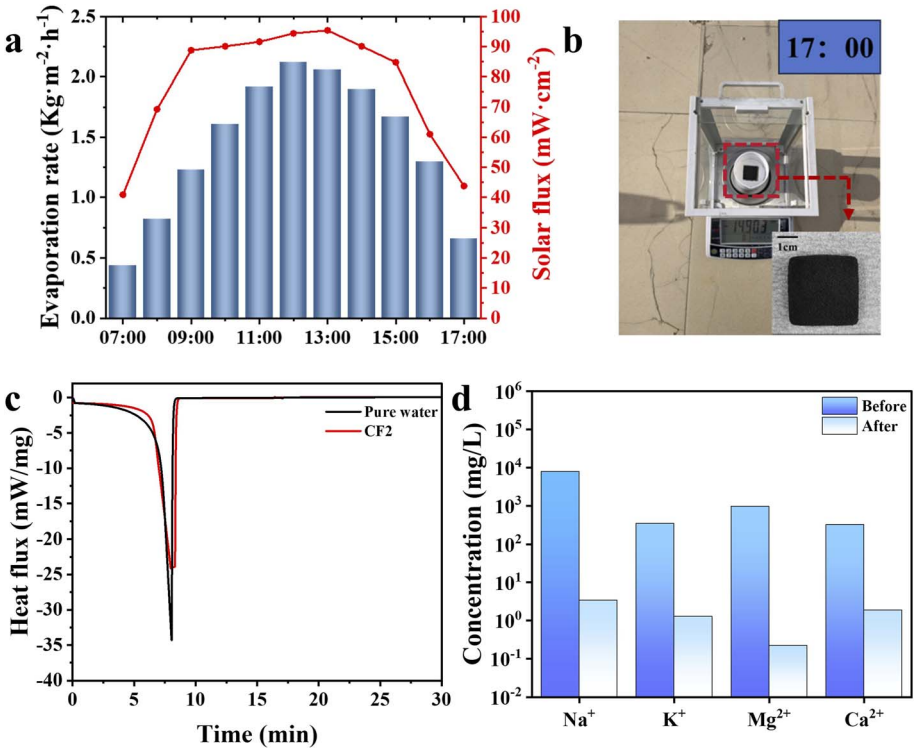

Fig. 7 (a) Evaporation rate of CF2 sample in outdoor experiments; (b) the photo of the CF2 sample outdoor experiment site taken at 17:00; (c) DSC curves for pure water and CF2 sample; (d) Na^+, K^+, Mg^{2+}, and Ca^{2+} concentrations of seawater before and after desalination.

within 0.02 seconds, confirming their excellent hydrophilic properties.

3.3 Desalination practicality

To assess the practical applicability of CF2, an outdoor experiment was conducted and the results are presented in Fig. 7(a and b). As shown in Fig. 7(a), the evaporation rate of the CF2 sample exhibited an upward trend from 7:00 to 12:00, correlating with increasing light intensity. During this period, the evaporation rate increased from 0.44 to 2.12 kg m^{-2} h^{-1}. Conversely, from 12:00 to 17:00, with decreasing light intensity, the evaporation rate exhibited a decreasing trend, decreasing from 2.12 to 0.66 kg m^{-2} h^{-1}. These observations clearly demonstrate the significant influence of light intensity on the evaporation rate of CF2. Furthermore, Fig. 7(b) shows that the CF2 sample did not exhibit salt crystal precipitation on its surface during 11 hours of continuous outdoor operation.

The evaporation enthalpy of pure water and the CF2 sample was measured *via* differential scanning calorimetry (DSC), and the evaporation efficiency of the CF2 sample was calculated. As shown in Fig. 7(c), the presence of CF2 resulted in a notable reduction in the evaporation enthalpy of water. The calculated evaporation efficiency of CF2 reached 90.59%. To evaluate the quality of freshwater collected by the CF2 evaporator, the concentrations of Na^+, K^+, Mg^{2+}, and Ca^{2+} in natural seawater from Qingdao were analyzed using inductively coupled plasma mass spectrometry (ICP-MS). The results are presented in Fig. 7(d). The concentrations of Na^+, K^+, Mg^{2+}, and Ca^{2+} decreased from 7805.28, 339.08, 948.90, and 314.80 mg L^{-1} before desalination to 3.36, 1.25, 0.22, and 1.85 mg L^{-1} after desalination, respectively. The corresponding removal efficiencies were 99.99%, 99.97%, 99.89%, and 99.90%, 99.89%, 99.90% and 97.78%, which were significantly higher than the baseline level of drinking water set by the World Health Organization. These results demonstrate the exceptional performance of the CF2 evaporator in achieving high desalination efficiency. Therefore, the CF2 evaporator exhibits great potential for practical applications in interfacial solar-powered desalination systems.

4 Conclusion

A high-efficiency solar interfacial evaporator (CF2) was successfully prepared using a co-carbonization process of lignin and petroleum asphalt. The CF2 exhibits exceptional performance in interface solar seawater desalination, characterized by low thermal conductivity (0.093 W m^{-1} K^{-1}), superior light absorption (93.31%) and outstanding compressive strength (10.62 MPa). These properties enable efficient solar-to-thermal energy conversion, localized heat concentration, and ensure durability in harsh marine environments. Under 1 standard sunlight, the evaporation rate of the CF2 evaporator in pure water reached 2.04 kg m^{-2} h^{-1}, achieving an evaporation efficiency of 90.59%. The hydrophilic and water-conducting properties of CF2 ensure a continuous water supply during the evaporation process. Notably, during continuous outdoor operation for 11 hours, the CF2 evaporator maintained consistent performance without any salt crystal deposition on its

surface. The generated fresh water met the drinking water standards established by the WHO. Furthermore, the preparation method of CF2 enables high-value utilization of industrial and agricultural waste, reducing reliance on non-renewable or costly precursors.

Author contributions

Jiawei Shang: conceptualization, writing – original draft. Wangda Qu: data curation, resources. Chen Liang: data curation. Linghong Yin: resources. Ming Li: conceptualization, funding acquisition, supervision, writing-review & editing. Jing Liu: resources.

Conflicts of interest

The authors declare that they have no known competing financial interests or personal relationships that could have appeared to influence the work reported in this paper.

Data availability

The data supporting this article has been included within the article. Supplementary information (SI): additional structural characterization figures, experimental optimization data, and performance comparison tables. See DOI: https://doi.org/10.1039/d5ra10093c.

Acknowledgements

The authors would like to acknowledge the funding support from Postdoctoral Science Foundation of China (2023M742136), Postdoctoral Creative Foundation of Shandong Province (SDCX-ZG-202400269) and Natural Science Foundation of Shandong Province (ZR2024MB109 and ZR2024QB047).

References

1 J. Y. Lu, Z. Q. Bu, Y. Q. Lei, D. Wang, B. He, J. Wang and W. T. Huang, Facile microwave-assisted synthesis of Sb_2O_3-CuO nanocomposites for catalytic degradation of p-nitrophenol, *J. Mol. Liq.*, 2024, **409**, 125503.
2 T. Li, G. He, Z. Jiang, Y. Duan and M. Liu, Research advances and new insights into multi-source solid waste-derived ceramic foams, *Sustainable Mater. Technol.*, 2025, **45**, e01535.
3 J. Xiao, T. Zhang, Z. Shi and S. Dong, Application and research progress of aerogel-based interfacial evaporation in solar desalination technology, *J. Environ. Chem. Eng.*, 2025, **13**, 117490.
4 P. Guo, R. Xue, Q. Zou, X. Ma, C. Su, Z. Zeng and L. Li, Enhanced Ultramicropore of Biomass-Derived Porous Carbon for Efficient and Low-Energy CO_2 Capture: Integration of Adsorption and Solar Desorption, *Energy Environ. Mater.*, 2025, e70140.
5 J. Ding, M. R. Templeton, Y. He, C. Peng and W. Chu, Optimizing multi-cycle atmospheric water harvesting *via* sorbent utilization efficiency, *Energy Environ. Sustainability*, 2025, **1**, 100025.
6 G. Xia, X. He, Y. Jia, Y. Zhu and Z. Tian, Design of a Cylindrical Thermal Rotary Concentrator Based on Transformation Thermodynamics, *Materials*, 2025, **18**, 4440.
7 Q. Shao, Y. Luo, M. Cao, X. Qiu and D. Zheng, Lignin with enhanced photothermal performance for the preparation of a sustainable solar-driven double-layer biomass evaporator, *Chem. Eng. J.*, 2023, **476**, 146678.
8 Q. Shao, Y. Li, Z. Liang, Z. Chen, A. Xu, X. Qiu and D. Zheng, Lignin: A multifunctional and sustainable photothermal material for solar-driven thermoelectric generation and desalination, *Composites, Part B*, 2024, **284**, 111694.
9 C. Zhang, J. Fang, X. Xu, M. Zhang, Z. Han and J. Liao, Al_2O_3/MgO-doped, CaO-based adsorbents for CO2 capture: A performance study, *Ann. N. Y. Acad. Sci.*, 2025, **1552**, 388–400.
10 Z. Chen, X. Jiang, Y. Boyjoo, L. Zhang, W. Li, L. Zhao, Y. Liu, Y. Zhang, J. Liu and X. Li, Nanoporous Carbon Materials Derived from Biomass Precursors: Sustainable Materials for Energy Conversion and Storage, *Electrochem. Energy Rev.*, 2024, **7**, 26.
11 Q. Zhou, Z. Liu, X. Wang, Y. Li, X. Qin, L. Guo, L. Zhou and W. Xu, Co_3S_4-pyrolysis lotus fiber flexible textile as a hybrid electrocatalyst for overall water splitting, *J. Energy Chem.*, 2024, **89**, 336–344.
12 W. Li, T. Li, B. Deng, T. Xu, G. Wang, W. Hu and C. Si, Fabrication of a facile self-floating lignin-based carbon Janus evaporators for efficient and stable solar desalination, *Adv. Compos. Hybrid Mater.*, 2024, **7**, 52.
13 Y. Xi, W. Guo, X. Wang, X. Lin and G. Lyu, Photothermal Properties and Solar Water Evaporation Performance of Lignin-Based Polyurethane Foam Composites, *Langmuir*, 2024, **40**, 7205–7214.
14 C. Liang, H. Xia, L. Yin, C. Du, X. Wu, J. Wang, S. Li, J. Xu, X. Zhang, Y. Wang and W. Qu, Carbon foam directly synthesized from industrial lignin powder as featured material for high efficiency solar evaporation, *Chem. Eng. J.*, 2024, **481**, 148375.
15 M. Porto, R. Angelico, P. Caputo, A. A. Abe, B. Teltayev and C. O. Rossi, The Structure of Bitumen: Conceptual Models and Experimental Evidences, *Materials*, 2022, **15**, 905.
16 L. Pan, Y. Wang, H. Hu, X. Li, J. Liu, L. Guan, W. Tian, X. Wang, Y. Li and M. Wu, 3D self-assembly synthesis of hierarchical porous carbon from petroleum asphalt for supercapacitors, *Carbon*, 2018, **134**, 345–353.
17 Y. Feng, H. Liu and Q. Lu, From non-carbon host toward carbon-free lithium-sulfur batteries, *Nano Res.*, 2024, **17**, 1337–1365.
18 K. Wacławiak, J. Myalski, D. N. Gurmu and G. G. Sirata, Experimental Analysis of the Mechanical Properties of Carbon Foams Under Quasi-Static Compressive Loads, *Materials*, 2024, **17**, 5605–5622.
19 Y. Liu, P. Li, Y. Wang, J. Liu, Y. Wang, J. Zhang, M. Wu and J. Qiu, A green and template recyclable approach to prepare Fe3O4/porous carbon from petroleum asphalt for lithium-ion batteries, *J. Alloys Compd.*, 2017, **695**, 2612–2618.

20 P. Abudu, L. Wang, M. Xu, D. Jia, X. Wang and L. Jia, Hierarchical porous carbon materials derived from petroleum pitch for high-performance supercapacitors, *Chem. Phys. Lett.*, 2018, **702**, 1–7.
21 K. Huo, Y. Sun, H. Jiang, S. Lin, H. Fang, Z. Cheng, S. Cao, L. Li, Y. Wang and M. Wu, Petroleum Pitch-Derived Porous Carbon Materials as Metal-Free Catalyst for Dry Reforming of Methane, *Molecules*, 2024, **29**, 4642–4661.
22 J. Samuel and S. Ok, Petroleum Asphaltene-Based Activated Nanoporous Carbon for CO2 Capture and H2 Storage, *Ind. Eng. Chem. Res.*, 2023, **62**, 9939–9950.
23 W. Qu, Z. Zhao, C. Liang, P. Hu and Z. Ma, Simple, additive-free, extra pressure-free process to direct convert lignin into carbon foams, *Int. J. Biol. Macromol.*, 2022, **209**, 692–702.
24 A. Abouelsaad and G. White, Comparing the Effect of Thermal-Oxidation and Photo-Oxidation of Asphalt Mixtures on the Rheological and Chemical Properties of Extracted Bituminous Binder, *Materials*, 2022, **15**, 6793–6808.
25 J. Yang, X. Wang, B. Shen, Z. Hu, L. Xu and S. Yang, Lignin from energy plant (Arundo donax): Pyrolysis kinetics, mechanism and pathway evaluation, *Renewable Energy*, 2020, **161**, 963–971.
26 D. Hu, X. Gu and B. Cui, Modeling the Oxidative Aging Kinetics and Pathways of Asphalt: A ReaxFF Molecular Dynamics Study, *Energy Fuels*, 2020, **34**, 3601–3613.
27 M. Sarnowski, K. J. Kowalski, J. B. Król and P. Radziszewski, Influence of Overheating Phenomenon on Bitumen and Asphalt Mixture Properties, *Materials*, 2019, **12**, 610–629.
28 X. Li, S. Liu, Y. Huang, Y. Zheng, D. P. Harper and Z. Zheng, Preparation and Foaming Mechanism of Pyrocarbon Foams Controlled by Activated Carbon as the Transplantation Core, *ACS Sustain. Chem. Eng.*, 2018, **6**, 3515–3524.
29 T. Chen, H. Xie, X. Qiao, S. Hao, Z. Wu, D. Sun, Z. Liu, F. Cao, B. Wu and X. Fang, Highly Anisotropic Corncob as an Efficient Solar Steam-Generation Device with Heat Localization and Rapid Water Transportation, *ACS Appl. Mater. Interfaces*, 2020, **12**, 50397–50405.
30 S. Jia, P. Chen, C. Wei, H. Tian and P. Yi, The connection between soil shrinkage and pore water distribution of compacted clays using the nuclear magnetic resonance technique, *Acta Geotech.*, 2024, **19**, 6039–6054.
31 S. Zhu, L. Kong, Y. Peng, Q. Zeng, B. Feng, O. Jian, P. Zhao, W. Zhang and Z. Li, Long-chain alkyl emulsifiers induced asphalt particle dispersion: Lipophilicity-enhancement effect, *Constr. Build. Mater.*, 2024, **449**, 138275–138289.
32 P. Xu, X. Zhu, P. Cong, X. Du and R. Zhang, Modification of alkyl group terminated hyperbranched polyester on paving epoxy asphalt, *Constr. Build. Mater.*, 2018, **165**, 295–302.
33 H. Yang, S. Cao, C. Wu, Z. Xi, J. Cai, Z. Yuan, J. Zhang and H. Xie, Bio-Based Polyurethane Asphalt Binder with Continuous Polymer-Phase Structure: Critical Role of Isocyanate Index in Governing Thermomechanical Performance and Phase Morphology, *Molecules*, 2025, **30**, 2466–2484.
34 F. Destyorini, Y. Irmawati, H. Widodo, D. S. Khaerudini and N. Indayaningsih, Properties and Performance of Gas Diffusion Layer PEMFC Derived from Coconut Coir, *J. Eng. Technol. Sci.*, 2018, **50**, 409–419.
35 X. Liu, D. D. Mishra, Y. Li, L. Gao, H. Peng, L. Zhang and C. Hu, Biomass-Derived Carbonaceous Materials with Multichannel Waterways for Solar-Driven Clean Water and Thermoelectric Power Generation, *ACS Sustain. Chem. Eng.*, 2021, **9**, 4571–4582.
36 S. Luo, J. Cao and A. G. McDonald, Cross-linking of technical lignin *via* esterification and thermally initiated free radical reaction, *Ind. Crops Prod.*, 2018, **121**, 169–179.
37 B. Tawiah, E. A. Ofori, D. Chen, Y. Ming, Y. Hou, H. Jia and B. Fei, Carbon-Based Thermal Management Solutions and Innovations for Improved Battery Safety: A Review, *Batteries*, 2025, **11**, 144.
38 J. Li, W. Liu, X. Qiu, X. Zhao, Z. Chen, M. Yan, Z. Fang, Z. Li, Z. Tu and J. Huang, Lignin: a sustainable photothermal block for smart elastomers, *Green Chem.*, 2022, **24**, 823–836.
39 D. N. Gurmu, K. Wacławiak and H. G. Lemu, Predicting the Compressive Properties of Carbon Foam Using Artificial Neural Networks, *Materials*, 2025, **18**, 2516–2537.
40 Y.-T. Chen, Y.-M. Sun, C.-C. Hu, J.-Y. Lai and Y.-L. Liu, Employing lignin in the formation of the selective layer of thin-film composite membranes for pervaporation desalination, *Mater. Adv.*, 2021, **2**, 3099–3106.
41 W. Wang, X. Chen, N. Bai, J. Zhu, C. Zhang, B. Cui, L. Chen, H. Wang, C. Kang, Y. Tang, Z. Li, D. Zhao, H. Niu and Z. Wang, Janus Structured Solar Evaporator with Intrinsic Salt Resistance towards High-Efficient Desalination, *J. Inorg. Organomet. Polym. Mater.*, 2025, **35**, 2515–2527.
42 S. K. Hazra, A. M. Saleque, A. K. Thakur, M. N. A. S. Ivan, D. Biswas, S. A. Khan, R. Saidur, Z. Ma and R. Sathyamurthy, Recent Advancement in Solar-Driven Interfacial Steam Generation for Desalination: A State-of-the-Art Review, *Energy Technol.*, 2024, **12**, 2301190–2301214.
43 L.-B. Zhong, S.-J. Chen, X. Hou, Q.-J. Zhang, C.-Y. Guo and Y.-M. Zheng, Salt-resistant carbon aerogel with hierarchical interconnected channels for continuous and efficient solar evaporation of hypersaline water, *Sci. China Mater.*, 2023, **66**, 3300–3309.
44 J. Yao, Q. Zhong, J. Zhang, J. Zhao and Z. Wang, Interfacial solar evaporation for zero liquid discharge desalination, *Commun. Mater.*, 2024, **5**, 1–15.
45 D. Barker-Rothschild, J. Chen, Z. Wan, S. Renneckar, I. Burgert, Y. Ding, Y. Lu and O. J. Rojas, Lignin-based porous carbon adsorbents for CO_2 capture, *Chem. Soc. Rev.*, 2025, **54**, 623–652.
46 P. S. Maria Balk, T. N. Axel and N. Tirelli, Lignin, the Lignification Process, and Advanced, Lignin-Based Materials, *Int. J. Mol. Sci.*, 2023, **24**, 11668.
47 X. Dong, Y. Zhang, S. Shao, H. Li and X. Yan, Application of Lignin-Derived Carbon Materials in Adsorption and Separation, *Separations*, 2025, **12**, 88.
48 M. Jayathilake, S. Rudra, N. Akhtar and A. A. Christy, Characterization and Evaluation of Hydrothermal Liquefaction Char from Alkali Lignin in Subcritical Temperatures, *Materials*, 2021, **14**, 3024.

49 C. Liu, Q. Lu, J. Qu, W. Feng, A. Thomas, Y. Li, I. G. Gonzalez Martinez, C. Pan and D. Mikhailova, Operando Studies of Bismuth Nanoparticles Embedded in N, O-Doped Porous Carbon for High-Performance Potassium-Ion Hybrid Capacitor, *Small*, 2024, **20**, 2311253.
50 H. G. Kim, Y. S. Kim, L. K. Kwac, S.-H. Chae and H. K. Shin, Synthesis of Carbon Foam from Waste Artificial Marble Powder and Carboxymethyl Cellulose *via* Electron Beam Irradiation and Its Characterization, *Materials*, 2018, **11**, 469.
51 N. Huda, M. A. Whitney, M. H. Razmpoosh, A. P. Gerlich, J. Z. Wen and S. F. Corbin, How phase (α and γ) and porosity affect specific heat capacity and thermal conductivity of thermal storage alumina, *J. Am. Ceram. Soc.*, 2021, **104**, 1436–1447.
52 C. Xiao, J. Peng, Y. Jiao, Q. Shen, Y. Zhao, F. Zhao, H. Li and Q. Song, Strong and Tough Multilayer Heterogeneous Pyrocarbon Based Composites, *Adv. Funct. Mater.*, 2024, **34**, 2409881.
53 S. Lu, J. Ling, S. Liu, X. Li and J. Liu, Structural Properties of a Novel Modified Carbon Foam Derived from Pine Sawdust, *Forests*, 2025, **16**, 311.